POLITECNICO
MILANO 1863

Department of Aerospace Science and Technology
Spacecraft Attitude Dynamics Course
Prof. Franco Bernelli Zazzera
Academic Year 2023/2024

Attitude dynamics analysis and control system design for a 12U Cubesat

Group 10

Project 280

Francesco Ceglie - PC 10796659
Alessandro Massini - PC 10990413
Francesco Paolo - PC 10738374
Caterina Maria Irma Pilotto - PC 10764521

Abstract

The goal of the following report is to present the results concerning a control design realized for a 12U Cubesat whose mission can be assumed to be close to METEOSAT-like applications. The analysis of the attitude dynamics of the satellite has been conducted using Matlab and SIMULINK® software. Once specified the operational environment and the physical and geometrical properties of the satellite, the main relevant external torque acting on the system has been modeled and computed. Chosen the mounted sensors and the mission requirements, the control logic and features design has been undertaken in order to accomplish three operative phases: detumbling, slew maneuver to align the satellite axis to the desired configuration, and alignment retention. The controls implemented for all the three phases is based on linear proportional commands.

Personal Code	**Surname**	**Name**	**Bachelor**
10796659	Ceglie	Francesco	Aerospace Engineering - Politecnico di Torino
10990413	Massini	Alessandro	Aerospace Engineering - Politecnico di Torino
10738374	Paolo	Francesco	Aerospace Engineering - Politecnico di Milano
10764521	Pilotto	Caterina M.I.	Aerospace Engineering - Politecnico di Milano

Table 1: Team Members

	Assigned specification	**Modifications**	**Motivations for modifications**
Platform	12U CubeSat		
Attitude parameters	Direction cosines		
Mandatory sensors	Sun sensor	Horizon sensors, Gyroscopes	To esteem nadir pointing accuracy and for initial detumbling
Actuators	3 reaction wheels	4 thrusters	To carry out high velocity detumbling

Table 2: Project Specifications

Contents

1 Mission profile and satellite properties **1**

2 System modelling **2**
2.1 Dynamics of the spacecraft . . . 2
2.2 Kinematics . . . 2
2.3 External environment . . . 2
2.3.1 Magnetic disturbance torque . . . 2
2.3.2 Gravity gradient disturbance torque . . . 3

3 ADCS architecture choices **3**
3.1 Sensors . . . 3
3.1.1 Sun sensor . . . 4
3.1.2 Earth horizon sensor . . . 4
3.1.3 Gyroscope . . . 4
3.2 Actuators . . . 5
3.2.1 Reaction wheels . . . 5
3.2.2 Cold gas thrusters . . . 5
3.3 Attitude determination Algorithm . . . 6

4 Mission phases **7**
4.1 Detumbling . . . 7
4.1.1 Detumbling control law . . . 7
4.2 Scan phase . . . 8
4.3 Slew manoeuvre . . . 8
4.4 Tracking . . . 9

5 Simulation results **11**
5.1 Detumbling performances . . . 11
5.2 Slew manoeuvre and tracking performances . . . 11

6 Conclusions **14**

1 Mission profile and satellite properties

The selected orbit is a Sun-synchronous orbit whose Keplerian parameters are shown in Table 3and period is computed to be $T = 3025.8s$. The geometry of the CubeSat is illustrated in Figure

$a[km]$	e	$i[deg]$	$\Omega[deg]$	$\omega[deg]$	$\theta[deg]$
7177.4	0	98.6	90	0	0

Table 3: Orbit Keplerian elements

1a. It has been assumed an average density for a single cube unit of the body and for the solar panel respectively as $\rho_u = 1330\,kg/m^2$ and $\rho_p = 833\,kg/m^2$ with single solar panel dimensions of 0.4x0.2x0.01. The moments of inertia computed along the principal inertial axis for the presented configuration are the following:

$$I = \begin{bmatrix} 0.353 & 0 & 0 \\ 0 & 0.110 & 0 \\ 0 & 0 & 0.358 \end{bmatrix}$$

In order to achieve the scanning of the Earth surface within multiple orbit revolutions, the objective set for this kind of mission is Nadir pointing. To take advantage of minimum passive stability offered by the rotation around the z axis of the satellite the nominal condition to be reached from body frame perspective is

$$\boldsymbol{\omega} = \{0, 0, n\}$$

where n is the mean orbital angular velocity of the satellite.

The solar panels are approximately faced towards the Sun for the entire orbit revolution allowing the onboard electrical devices to be recharged whenever needed. Undoubtedly the large surface of recharge configuration will affect the orbital elements due to the effect of external forces such as Sun radiation pressure and air drag since the satellite operates in an LEO environment: this makes a deployment system necessary. Nevertheless, the reference designing condition taken in this study is the one presenting the largest moment of inertia, taking for granted that equilibrium would be ensured even in other configuration where the satellite moment shrinks.

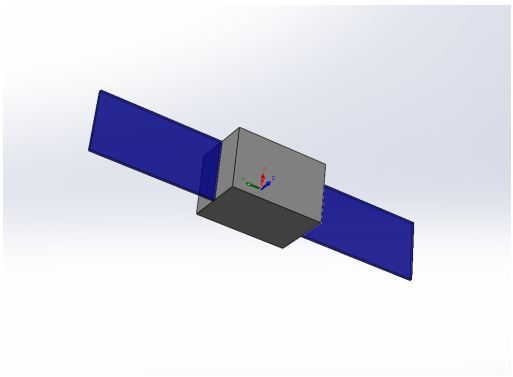

(a) Mock up of the satellite

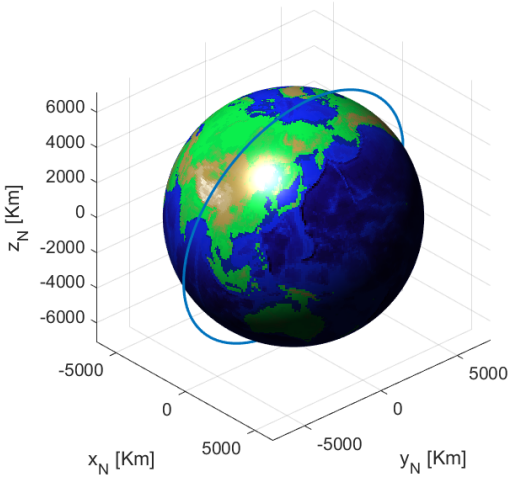

(b) Sun-synchronous orbit

Figure 1

2 System modelling

To simulate the physical behavior of both spacecraft and environment various Simulink subsystems that will be discussed in the following paragraphs have been implemented.

2.1 Dynamics of the spacecraft

The satellite attitude dynamics can be obtained from the numerical integration of the Euler's equation:

$$I\dot{\boldsymbol{\omega}} = \boldsymbol{\omega} \wedge I\boldsymbol{\omega} + \mathbf{M} \tag{1}$$

where I is the inertia matrix, $\boldsymbol{\omega}$ is the angular velocity expressed in body reference frame, and $\mathbf{M}$ is the external torque that includes two contributions of external disturbances and control torque provided by the actuators.

The spacecraft space disposal is retrieved via integration of the equation of motion in the Two Body problem referring to Keplerian coordinates, neglecting the presence of orbit perturbation since the limited simulation time chosen for conducting the analysis does not allow us to perceive any significant variation on such a scale.

2.2 Kinematics

The tracking of the body axes rotation with respect to the Earth centered inertial reference frame is fulfilled with rotation matrices $A_{B/N}$. Assuming small progressive rotation for the body frame over time, the evolution of the rotation matrix can be computed by integrating the following relation:

$$\dot{A} = -[\boldsymbol{\omega}\wedge]A \tag{2}$$

where$[(\cdot)\wedge]$ is the skew operator.

The computation of A matrix through numerical approach leads itself to become non-orthogonal due to numerical error accumulating. To prevent this the A matrix can be orthogonalized through an iterative process carried out at each integration step. For our applications is sufficient to arrest this iteration to the first order so that the re-orthogonalized matrix can be expressed as

$$A_1 = \frac{3}{2}A_0 - \frac{1}{2}A_0 A_0^T A_0 \tag{3}$$

2.3 External environment

The most relevant disturbances acting on spacecraft attitude dynamics in the established operative conditions are the gravity gradient torque and the magnetic torque. As previously mentioned, the air drag and the solar radiation pressure disturbance would play a key role in a long period analysis of trajectory perturbations. Since the satellite is symmetric with respect to the three body reference planes, these last two contributions can be considered negligible in terms of torques applied to the system.

2.3.1 Magnetic disturbance torque

The magnetic field of the Earth represents the first source of disturbance while interacting with residual magnetic dipole of the spacecraft. Due to electromagnetic phenomena the torque acting on the spacecraft can be computed as $\mathbf{M} = \mathbf{m}\wedge\mathbf{B}_B$ where the residual magnetic dipole is assumed constant and equal to $\mathbf{m} = \big[0.04, 0.03, 0.07\big] Am^2$ and $\mathbf{B}_B$ is the geomagnetic field described in body reference frame. The latter has been modeled through the gradient of a scalar potential V, expressed as a series expansion of spherical harmonics in the Earth centered equatorial reference frame and then rotated using body frame rotation matrices. The function used to do so is reported in [1] where the coefficients considered refer to the IGRF model of 13^{th} Gen 2020. For this work, an approximation including terms up to the fourth order has been considered to be sufficiently accurate.

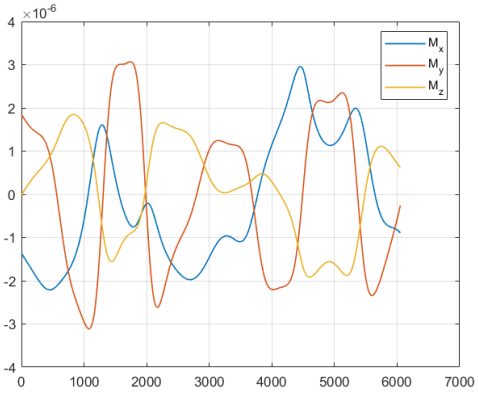

Figure 2: Magnetic disturbance torque over an uncontrolled orbit

2.3.2 Gravity gradient disturbance torque

The other disturbing torque taken into account in the analysis is the gravity gradient. Its magnitude isn't that intense if compared with the other one, anyway, due to the relevant mean angular LEO velocity and the inertia moments of recharging configuration that are relatively different, its contribution could become not completely negligible. It can be expressed by the following relation:

$$\mathbf{M} = 3n^2 \begin{bmatrix} (I_z - I_x)c_2c_3 \\ (I_x - I_z)c_1c_3 \\ (I_y - I_x)c_1c_2 \end{bmatrix} \tag{4}$$

where the vector $[c_1, c_2, c_3]$ contains the direction cosines of the three body axes with respect to the radial direction expressed by the yaw axis in the LVLH frame.

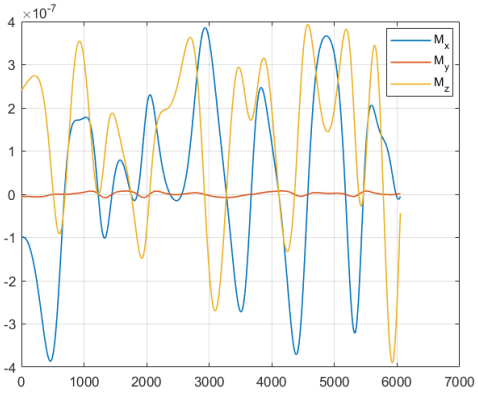

Figure 3: Gravity gradient torque over an uncontrolled orbit

3 ADCS architecture choices

3.1 Sensors

Sensors are the eyes of the satellite, they allow the onboard computer to retrieve information about the actual attitude of the system, with a certain accuracy and sample time, by their output signals.

3.1.1 Sun sensor

SSOC-D60 [2] is a digital Sun sensor that returns the body frame unitary vector of the Sun position. In particular, through a system of photodiodes, it measures the angles of incidence of the Sun rays on its surface as shown in Figure 4 by detecting the intensity of the incoming radiation.

The specifications of its performances are reported in Table 4. The entity of the noise error affecting the returned value is expressed by the accuracy and has been modeled in Simulink through a white noise whose power intensity is equal to

$$W = \frac{(Accuracy/3)^2}{Sampling frequency}$$

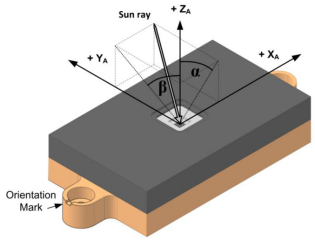

Figure 4: Sun sensor reference

Sampling frequency$[Hz]$	Accuracy$[deg]$	Sensitivity$[deg]$	FOV$[deg]$
50	0.3	0.05	60

Table 4: Sun sensor specifications

3.1.2 Earth horizon sensor

The selected sensor to provide an estimation of the nadir pointing accuracy is the CubeSense Earth Gen2 [3] whose performance parameters are reported in Table 5. By measuring the infrared radiation this device is able to return the value of the nadir direction within a certain precision field. In the Simulink model, this sensor output has been modeled taking the expression of $-\mathbf{r}_N$ position of the satellite from orbit propagation, rotating it in body frame, and adding noise to the signal. The electrical error inserted has been modeled with a white noise whose injection power is the same used for the Sun sensor.

Sampling frequency$[Hz]$	Accuracy$[deg]$	Sensitivity$[deg]$	FOV$[deg]$
2	0.1	0.1	80

Table 5: Earth horizon sensor specifications

3.1.3 Gyroscope

The gyroscope chosen to provide angular velocity measurements during the detumbling and slew maneuvers is the STIM202 module [4], a MEMS-based 3-axis gyroscope, in order to save as much space and weight as possible. Its specifications are shown in table 6. The noise that affects the measurements has been modeled in Simulink via a white noise with an intensity equal to $W = ARW^2$, where the angular random walk parameter is expressed in $[rad/\sqrt{s}]$.

Sampling frequency$[Hz]$	Accuracy$[deg/hour]$	ARW $[deg/\sqrt{hour}]$	Full scale $[deg/s]$
10 (max 1000)	0.22	0.17	± 400

Table 6: Gyroscope specifications

3.2 Actuators

The model of the actuators is essential to convert the feedback control torque computed by the onboard control logic into a physical quantity acting on the spacecraft and entering the Euler's equation. The required actuators to accomplish all the analyzed mission phases are a set of reaction wheels and thrusters.

3.2.1 Reaction wheels

The reaction wheel used in the analysis presents performances similar to the RocketLab 30 [5], they are reported in Table 7. Even if this specific system can be controlled using only two actuators, for mission requirements a set of three reaction wheels in body frame layout has been considered to perform the latest part of detumbling and the tracking phase. The RWs generated torque exchanged with the spacecraft comes from their angular acceleration: once computed the control torque $\mathbf{M}_c$ from the onboard logic, the torque that the actuators has to provide to satisfy that command can be obtained from:

$$\dot{\mathbf{h}_r} = -A_r^* \left[\boldsymbol{\omega} \wedge I\boldsymbol{\omega} + \boldsymbol{\omega} \wedge A_r \mathbf{h}_r + \mathbf{M}_c \right] \tag{5}$$

where $\mathbf{h}_r$ is a [3x1] vector containing the angular momentum of the reaction wheels around their fixed rotation axis (measured with an integrated sensor) and A_r is a [3x3] matrix whose columns contain the direction cosines of the relative reaction wheel rotation axis with respect to the body frame, in this analyzed configuration it coincides with an identity matrix.

Dimensions$[mm]$	Inertia$[kg\,m^2]$	Saturation speed$[rad/s]$	Maximum torque$[Nm]$
50x50x40	$5.78e{-}5$	500	0.002

Table 7: Single RW specifications

3.2.2 Cold gas thrusters

The VACCO industries cold gas thrusters [6] have been proposed as the actuators to be employed in the detumbling maneuver that the satellite must perform right after orbit injection and to allow the desaturation of the reaction wheels. The chosen thrusters do not allow the possibility to adjust the intensity of the produced thrust: only a simple on-off control is applicable. In order to reduce the weight of the chosen assembly, shown in Figure 5 [1], employs only four thrusters. Nevertheless, by switching on different combinations of two thrusters, it is able to provide a torque around any of the body axes with the required sign. The torque $\mathbf{M_{thr}}$ produced by the thrusters, as reported in [7] is given by:

$$\mathbf{M_{thr}} = T_{thr}\mathbf{f} \tag{6}$$

Where $\mathbf{f}$ is the [4x1] vector of the real force intensities given by the four thrusters and T_{thr} is the following matrix, with $l = 0.15m$, $x = 0.05m$, $\alpha = 30\,\text{deg}$. In order to simulate the imperfections and the oscillations in the delivery of the gas to the nozzle, a white noise disturbance has been added to the ideal force signal.

$$T_{thr} = \begin{bmatrix} lsin\alpha & lsin\alpha & -lsin\alpha & -lsin\alpha \\ -x(sin\alpha - cos\alpha) & x(sin\alpha - cos\alpha) & -x(sin\alpha - cos\alpha) & x(sin\alpha - cos\alpha) \\ -lcos\alpha & lcos\alpha & lcos\alpha & -lcos\alpha \end{bmatrix} \tag{7}$$

[1] The body frame used in the report's analysis is rotated by 90 degrees around the $-x$ axis with respect to the one depicted in the figure.

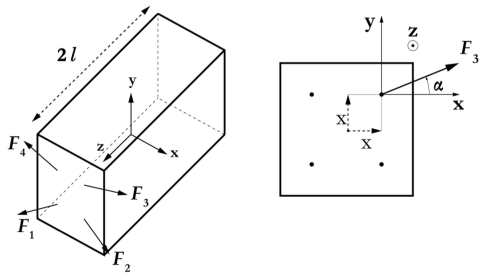

Figure 5: Thrusters configuration

Nominal force[N]	Specific impulse[s]	Total impulse [Ns]	Noise intensity
0.01	40	103	1e-8

Table 8: Single thruster specifications

3.3 Attitude determination Algorithm

The two measurements from the Sun and Earth horizon sensors are exploited to compute an attitude direction cosine matrix through a simple algebraic algorithm, which was found to be reasonably accurate. If we call $\mathbf{r_{S}}_B$ and $\mathbf{r_{S}}_N$ the normalized vectors that respectively express the position of the Sun in body and inertial frames, and $\mathbf{r_{E}}_N$, $\mathbf{r_{E}}_N$ the ones that express the position of the Earth in body and inertial frame, then the attitude determination algorithm is the following:

$$\begin{aligned} \mathbf{s_1} &= \mathbf{r_{S}}_N; \\ \mathbf{s_2} &= \frac{\mathbf{r_{S}}_B \wedge \mathbf{r_{E}}_B}{\left|\mathbf{r_{S}}_N \wedge \mathbf{r_{E}}_B\right|}; \\ \mathbf{s_3} &= \mathbf{s_1} \wedge \mathbf{s_2}; \end{aligned} \tag{8}$$

Therefore the S matrix is assembled by concatenating these three column vectors:

$$S = [\mathbf{s_1}, \mathbf{s_2}, \mathbf{s_3}]$$

The same process is carried out for the two inertial frame measurements and the V matrix is assembled:

$$\begin{aligned} \mathbf{v_1} &= \mathbf{r_{S}}_N; \\ \mathbf{v_2} &= \frac{\mathbf{r_{S}}_N \wedge \mathbf{r_{E}}_N}{\left|\mathbf{r_{S}}_N \wedge \mathbf{r_{E}}_N\right|}; \\ \mathbf{v_3} &= \mathbf{v_1} \wedge \mathbf{v_2}; \\ V &= [\mathbf{v_1}, \mathbf{v_2}, \mathbf{v_3}] \end{aligned} \tag{9}$$

Then, considering that S and V are related to each other through the direction cosines matrix that expresses the attitude of the satellite:

$$S = A_{B/N} V \tag{10}$$

and exploiting the fact that the V matrix is orthonormal the attitude DCM can be simply computed as:

$$A_{B/N} = S V^T \tag{11}$$

Note that in equation 8 the Sun position measurement has been chosen as the first vector to be put in the S matrix because the Sun sensor has a higher precision compared to the Earth horizon one.

4 Mission phases

The ADCS system of the cubesat is able to cover all phases of

4.1 Detumbling

As the satellite detaches from the launch vehicle, it is injected into its orbit with a relatively high random angular velocity, which must be reduced prior to the beginning of the pointing and tracking phases. Therefore, it is necessary to design an appropriate detumbling maneuver. The main challenge the authors faced in this process was the fact that the chosen reaction wheels were too small to reduce the angular velocity of the satellite to an acceptable value (e.g. 10e-4 rad/s): they would already run into saturation at the beginning of the detumbling maneuver. In fact, the literature confirms that they are mostly used for fine tracking control. For this reason, together with the fact that increasing the size of the reaction wheels was not feasible due to the size and weight constraints of the given spacecraft, there was the necessity to add another set of actuators to the cubesat.

In addition to that, at injection into orbit one or both sensors will likely have their target (Earth and/or Sun) outside their field of view. Therefore the satellite would not be able to determine its attitude, and as a consequence its angular velocity. Consequentially, the set of sensors used in the tracking phase is not usable for the detumbling phase.

The first option considered by the authors was to employ a three axis magnetorquer coupled with a three axis magnetometer. This set of sensors and actuators would exploit the so called b-dot control law, which is a common solution for small cubesats operating in Low Earth Orbits.

However, the size of the given cubesat sits at the upper limit of the satellites that most of the magnetorquers found on the market are able to properly detumble. This consideration, coupled with the fact that the chosen orbit sits at a higher altitude than the Low Earth Orbits that are usually considered for the b-dot law, led to this possibility being discarded.

The chosen set of sensors/actuators employed in the detumbling phase is a gyroscope and a set of four cold gas thrusters, whose characteristics have been described in Sections 3.1 and 3.2. The main goal was to minimize size and weight, hence the choice of a lightweight MEMS gyroscope and of the minimum set of thrusters able to provide a torque around any of the body axes.

4.1.1 Detumbling control law

In this phase, via the Lyapunov control theory it is possible to choose the kinetic energy as the Lyapunov function:

$$L(\omega) = \frac{1}{2}(I_x\omega_x^2 + I_y\omega_y^2 + I_z\omega_z^2) \tag{12}$$

$$\dot{L}(\omega) = (I_x\omega\dot{\omega}_x + I_y\omega\dot{\omega}_y + I_z\omega\dot{\omega}_z)$$

Then, by substituting the Euler equations:

$$\dot{L}(\omega) = (M_x\omega_x + M_y\omega_y + M_z\omega_z)$$

and choosing:

$$\mathbf{M} = -k\boldsymbol{\omega} \tag{13}$$

we obtain that $\dot{L}$ is negative for any value of ω and the equilibrium point is $\omega = 0$.

Since the detumbling initial angular velocity is too high to get reduced only through the reaction wheels due to the occurrence of saturation, the initial part of the detumbling is carried out by the thrusters. The goal of this phase is to reduce the angular velocity of the cubesat to values small enough to be taken care by the reaction wheels, which in turn will execute the final reduction of the angular velocity to a "reasonably small" value. Due to the on-off nature of the thrusters and considering that the chosen configuration can apply a torque around only one body

axis at a time it was necessary to modify the "classic" detumbling law, obtaining the following logic-based control:

$$\mathbf{u}_{ideal} = -\mathbf{M}_{i_{max}} sign(\omega_{i_{max}}) \mathbf{e}_{i_{max}} \tag{14}$$

where e_i with $i = 1, 2, 3$ are the body axes and i_{max} is defined as:

$$i_{max} = arg_i(max|\omega_i|) \tag{15}$$

The nominal torque values produced by the thrusters around each axis are given by:

$$M = \begin{Bmatrix} 2lFsin\alpha \\ 2xF(cos\alpha - sin\alpha) \\ 2lFcos\alpha \end{Bmatrix} \tag{16}$$

After each component of the angular velocity stabilizes below a threshold value of $0.02 rad/s$, the control is passed to the reaction wheels. In this case, the control law becomes again the "classical" one defined by Lyapunov's theory, with a gain $k = 0.1$:

$$\mathbf{u}_{ideal} = -k\boldsymbol{\omega} \tag{17}$$

In order to provide a usable measurement to the onboard controller of the satellite it was necessary to filter the output signal of the gyroscopes with a discrete low pass filter, designed via a spectral analysis of the angular velocities of the satellite in an uncontrolled condition. In addition to that, the sampling frequency of the gyroscope has been limited to 10 Hz to further reduce the noise.

4.2 Scan phase

At the end of the detumbling the spacecraft can assume any arbitrary orientation, for this reason, one or both the Sun and the horizon sensor can be incapable of providing an output since their reference object could lie out of their field of view. In order to proceed to the slew maneuver and the tracking phase by having only these two types of onboard sensors, a re-orienteering maneuver is needed to have them supplying the attitude determination algorithm and to esteem the misalignment between the target and the current body frame. One approximated way to accomplish this objective can be to slowly rotate the spacecraft around one of its axes shortly after the point when one of the two sensors provides a non null output, once reached this condition another rotation around the "switched-on" sensor axis is needed to search for a useful orientation of the other sensor.

Whereas this procedure is not the main goal of the treated analysis, this particular phase has not been modeled nor tested, taking for granted its feasibility considering the spacecraft available tools discussed up to now. Nevertheless, it has been supposed that this maneuver shall bring the spacecraft to the same exit velocities condition obtained at the end of detumbling by knowing the orientation of the satellite with respect to the LVLH target frame since the sensors are working properly by this time.

4.3 Slew manoeuvre

Once relying on the Sun and horizon sensors output to determine the orientation of the satellite, it is necessary to perform a large angle rotation to make the body axes closer to the pointing target ones. For this purpose, a slew maneuver based on the same proportional command that will be presented in Section 4.4 has been chosen.

In this case the off-diagonal terms of $A_{B/L}$ error matrix, expressing the rotation of the body axes with respect to the LVLH frame, can't be assumed to be close to the misalignment error angles α_x, α_y and α_z themselves but represent the dot product between cross unitary vectors of

the target frame with respect to the body frame and vice versa. As previously said, the tracking control law can be extended to large rotations by substituting the variable related to the angle with the corresponding term figuring in the error matrix. Since the implemented controller is based on a linear PID logic, during the slew maneuver the command onto the velocities measured through gyroscopes is given directly in body reference so that the relative control variable results to be $[\omega_x, \omega_y, \omega_z - n]$, while the command onto the "large angles" and their integral is given in terms of error quantities between the LVLH frame and the satellite one.

It is worth mentioning the fact that, at this mission stage, the slew maneuver can be carried out without the usage of gyroscope sensors but by employing a state observer that will be discussed in the following paragraph and through which it can be retrieved a raw estimation of the system state, at least in this transition phase. The choice to take on the first discussed method has to be imputed to the fact that it allows to reach the steady state far before than a proportional command based on the coarse state.

4.4 Tracking

When the target state condition is reached, it is necessary to maintain it over the entire orbit. In this phase, the 3 reaction wheels have been used to provide better pointing accuracy, together with a state feedback control logic operating through a PID representation of the state space. The state variables of the system are obtained from the output of the Sun and horizon sensors only thanks to a state observer implemented to retrieve the velocities and the integral of the angles.

For a body orientation not so distant from the desired equilibrium configuration the system can be represented through the following linearized state space model referring to the error quantities between the LVLH frame and the body frame:

$$\begin{cases} \dot{\mathbf{x}} = A\mathbf{x} + B\mathbf{u} \\ \mathbf{y} = C\mathbf{x} \end{cases}$$

where $\mathbf{u}$ is the control input variable expressing the torque that has to be applied to the system along each axis to guarantee stability, $\mathbf{y}$ is the sensor outputs available onboard, while the state vector and the matrices figuring in the equation are the following

$$\mathbf{x} = \begin{Bmatrix} \dot{\alpha_x} \\ \dot{\alpha_y} \\ \dot{\alpha_z} \\ \alpha_x \\ \alpha_y \\ \alpha_z \\ \int \alpha_x \\ \int \alpha_y \\ \int \alpha_z \end{Bmatrix}$$

$$A = \begin{bmatrix} 0 & (1-K_{yaw})n & 0 & -K_{yaw}n^2 & 0 & 0 & 0 & 0 & 0 \\ (K_{roll}-1)n & 0 & 0 & 0 & -4K_{roll}n^2 & 0 & 0 & 0 & 0 \\ 0 & 0 & 0 & 0 & 0 & -3K_{pitch}n^2 & 0 & 0 & 0 \\ 1 & 0 & 0 & 0 & 0 & 0 & 0 & 0 & 0 \\ 0 & 1 & 0 & 0 & 0 & 0 & 0 & 0 & 0 \\ 0 & 0 & 1 & 0 & 0 & 0 & 0 & 0 & 0 \\ 0 & 0 & 0 & 1 & 0 & 0 & 0 & 0 & 0 \\ 0 & 0 & 0 & 0 & 1 & 0 & 0 & 0 & 0 \\ 0 & 0 & 0 & 0 & 0 & 1 & 0 & 0 & 0 \end{bmatrix}$$

$$B = \begin{bmatrix} \frac{1}{I_x} & 0 & 0 \\ 0 & \frac{1}{I_y} & 0 \\ 0 & 0 & \frac{1}{I_z} \\ 0 & 0 & 0 \\ 0 & 0 & 0 \\ 0 & 0 & 0 \\ 0 & 0 & 0 \\ 0 & 0 & 0 \\ 0 & 0 & 0 \end{bmatrix}$$

$$C = \begin{bmatrix} 0 & 0 & 0 & 1 & 0 & 0 & 0 & 0 & 0 \\ 0 & 0 & 0 & 0 & 1 & 0 & 0 & 0 & 0 \\ 0 & 0 & 0 & 0 & 0 & 1 & 0 & 0 & 0 \end{bmatrix}$$

It is important to remark the fact that the aim of this representation is to describe the physical behavior of the system in a linearized form to shape the control law in the most effective way and it is nothing more than a mathematical expedient. Note, in fact, that including the integral of the state angle variables the system results to be no longer observable. However, the integrated terms are crucial to deal with the equilibrium steady state errors since their action through the proportional command significantly improves the pointing accuracy. For this reason, the onboard observer has been built considering a reduced system that is able to return the following properly observed state:

$$\tilde{\hat{\mathbf{x}}} = \begin{Bmatrix} \hat{\dot{\alpha}}_x \\ \hat{\dot{\alpha}}_y \\ \hat{\dot{\alpha}}_z \\ \hat{\alpha}_x \\ \hat{\alpha}_y \\ \hat{\alpha}_z \end{Bmatrix}$$

The observer is a system capable of retrieving a state estimation of the real system through some information such as the sensor outputs as long as the associated observability matrix[2] is full rank. In the end, the integrals of the three observed angle variables are computed out of the observer subsystem through a simple integrator with null initial condition[3] and added to the state space vector in order to compute the PID proportional command $\mathbf{u} = -K\hat{\mathbf{x}}$.

To find the K matrix defining the proportional gain to generate the control action, a Linear Quadratic Regulator (LQR) has been implemented to find the optimal value of the previously mentioned matrix that minimizes the cost function

$$J = \int_0^\infty (\mathbf{x}^T Q \mathbf{x} + \mathbf{x}^T R \mathbf{x}) dt \tag{18}$$

where the Q and R matrices are weight matrices that have been defined starting from the Bryson's criteria and adapted through a trial and error process in order to obtain a good requirements satisfaction, also looking to the rotor supplied torque that is an indirect measure of RWs energy

[2] Defined as $N = \begin{bmatrix} C^T & A^T C^T & (A^T)^2 C^T & \dots & (A^T)^n C^T \end{bmatrix}$

[3] The null initial condition has been chosen since the integral of the angles coincides with the integral of the steady state error.

consumption:

$$Q = \begin{bmatrix} 0.1 & 0 & 0 & 0 & 0 & 0 & 0 & 0 & 0 \\ 0 & 0.1 & 0 & 0 & 0 & 0 & 0 & 0 & 0 \\ 0 & 0 & 0.1 & 0 & 0 & 0 & 0 & 0 & 0 \\ 0 & 0 & 0 & 0.01 & 0 & 0 & 0 & 0 & 0 \\ 0 & 0 & 0 & 0 & 0.01 & 0 & 0 & 0 & 0 \\ 0 & 0 & 0 & 0 & 0 & 0.01 & 0 & 0 & 0 \\ 0 & 0 & 0 & 0 & 0 & 0 & 0.001 & 0 & 0 \\ 0 & 0 & 0 & 0 & 0 & 0 & 0 & 0.001 & 0 \\ 0 & 0 & 0 & 0 & 0 & 0 & 0 & 0 & 0.001 \end{bmatrix}; \quad R = \frac{1}{(5e{-}4)^2} \begin{bmatrix} 1 & 0 & 0 \\ 0 & 1 & 0 \\ 0 & 0 & 1 \end{bmatrix}$$

Using the same criteria the poles of the error dynamics between the observed state and the real state have been selected and imposed through a pole placement technique: to guarantee a good filtering action of sensor noise together with a sufficient reactivity, the observer gain matrix L needs to make the error dynamics two times faster than the controlled system one.

5 Simulation results

In the current paragraph, the outcomes of the simulation will be presented and briefly commented for all the analyzed phases that have been previously discussed. The simulation has been run with an automatic fixed step solver and an integration step set to $0.01s$. Moreover, it has been divided into two different Simulink files: the first concerning the detumbling phase and the other one the slew maneuver and tracking phase.

5.1 Detumbling performances

The following angular velocity vector [7] has been chosen as the initial condition for the detumbling phase:

$$\boldsymbol{\omega} = \{0.45, 0.52, 0.55\}$$

In order to reduce fuel consumption a threshold angular velocity for the activation of thrusters has been chosen as $0.02 rad/s$ for each of its components. At $t = 300s$, right after this condition is reached, the thrusters are turned off and the reaction wheels take control of the detumbling. The total impulse expended by thrusters is:

$$I_{tot} = \sum_{k=1}^{4} \int_0^{300} F_k \, dt = 16.16 Ns \tag{19}$$

As shown in figure 7, they are able to further reduce the angular velocities down to values in the range of $\pm 10^{-4} rad/s$, for which the detumbling can be considered complete. The whole process takes place in around 320 seconds.

The noise introduced by the gyroscopes, of course, disturbs the measured values of ω with respect to the real ones. In fact it was necessary to both filter the measurements and reduce its sample rate from This phenomena becomes more relevant when the velocities become small but does not deteriorate the performance of the detumbling significantly , as shown in figure

The angular velocities during the detumbling phase are shown in figure 6, and a detailed view of their final values is given in figure.

5.2 Slew manoeuvre and tracking performances

The initial condition on the angular velocities for the slew manoeuvre has been considered as the exit one guaranteed by the detumbling phase:

$$\boldsymbol{\omega} = \{1.5e{-}4, 1e{-}4, 1e{-}4\}$$

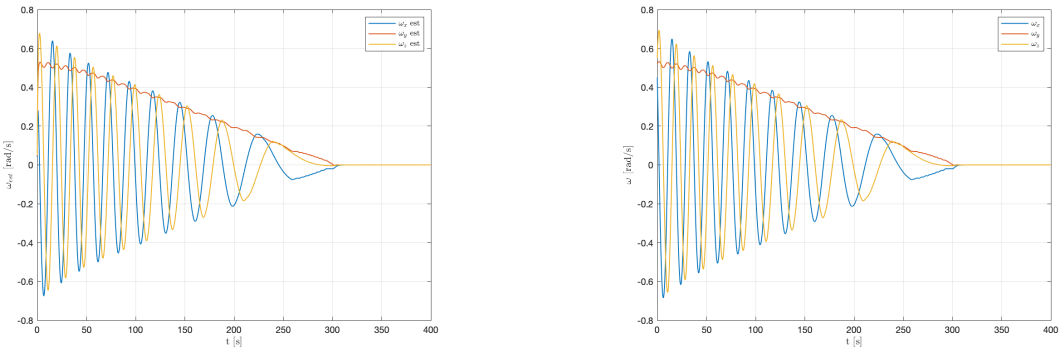

(a) Observed velocities (b) Real velocities

Figure 6: Angular velocities during the detumbling phase

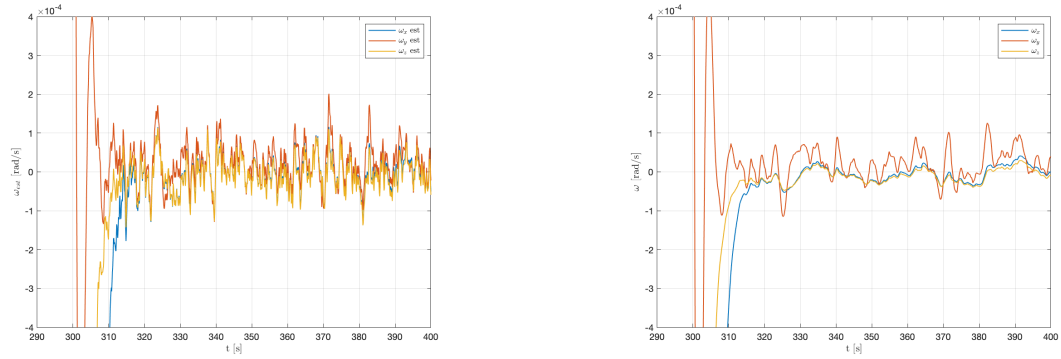

(a) Observed velocities (b) Real velocities

Figure 7: Final detumbling angular velocities

The starting orientation of the satellite has been chosen so that the Sun and horizon sensor can return a meaningful output and the error matrix can be computed through the attitude determination algorithm:

$$A_{B/N}(0) = \begin{bmatrix} 0.074 & 0.866 & 0.494 \\ 0.790 & -0.353 & 0.499 \\ 0.607 & 0.353 & -0.711 \end{bmatrix}$$

As shown in Figure 8 the slew maneuver can be considered to be accomplished within a time of $300s$, it is worth to remark the fact that the observed velocities result to be far more similar to the real ones during the slew maneuver phase because they are measured directly through the gyroscope. Regarding the tracking phase, the observer has been switched on $50s$ in advance the tracking command begins to be supplied to actuators in order to ensure the stabilization of the error between observed and real state. It is remarkable that the real performances do not result worsening, even if the observed velocities are not exactly reproducing the real condition of the system at least for what concerns the velocities. The cause of this behavior can be attributed to the fact that the observer poles do not guarantee sufficiently fast error dynamics. On the other hand having chosen such "slow" poles drastically reduces the actuators energy consumption as denoted in Figure 9 without a significant loss of pointing accuracy: the maximum real pointing error goes from $0.5730°$ to $0.8594°$, a precision grade that can be fairly accepted for this kind of mission. The benefit of a slower observer, beside to concerning an energy saving, is to influence

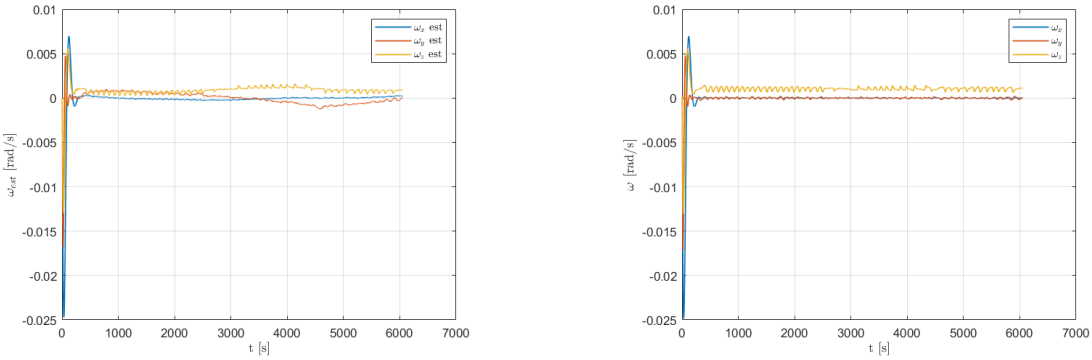

(a) Observed velocities

(b) Real velocities

Figure 8: Velocities in the body frame

the wear of the actuators lengthening the spacecraft operative lifetime.

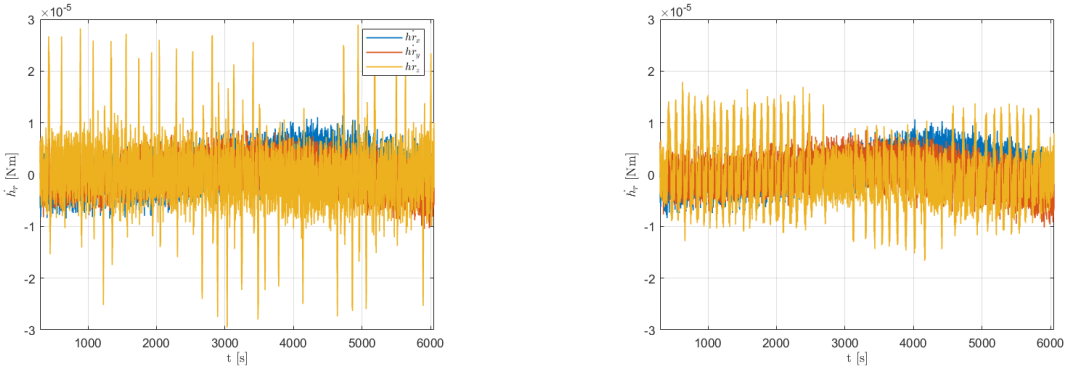

(a) Rotor torque with a five times faster observer

(b) Rotor torque with a two times faster observer

Figure 9: Comparison between supplied rotors torque

Figure 11 represents the observed and the real pointing error. Also, in this case, the observer does not provide a good prediction of the true state of the error angles and other poles configuration has been tested: making it faster would mean to soften its noise filtering power and this leads both the true and control velocity to oscillate with a greater frequency and amplitude[4], moreover the pointing error floats within a shrunk range that presents not so relevant improvement with respect to the slow observer one.

[4]This behavior can affect some onboard instruments performances such as cameras and optical devices, i.e. images blurring

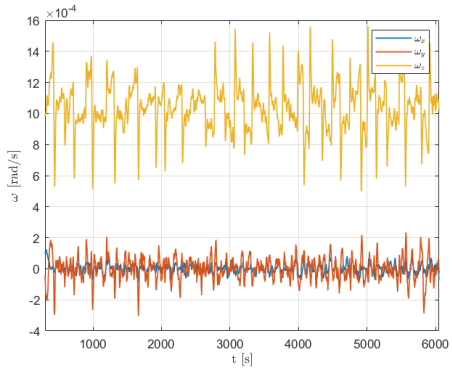

(a) Real velocities with a five times faster observer

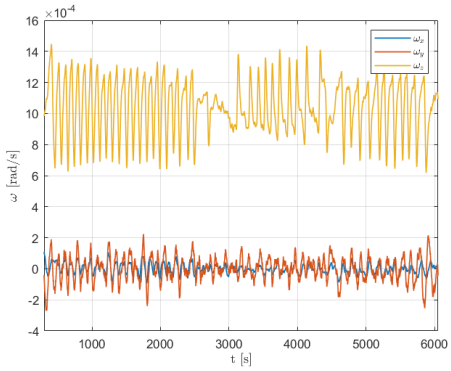

(b) Real velocities with a two times faster observer

Figure 10: Comparison between velocities

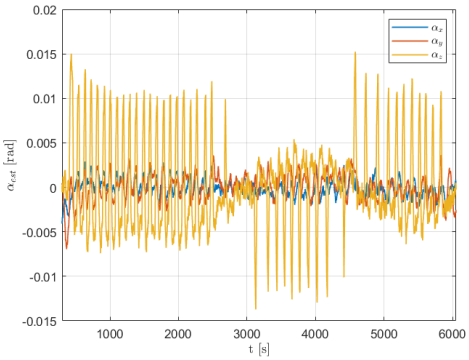

(a) Control pointing error

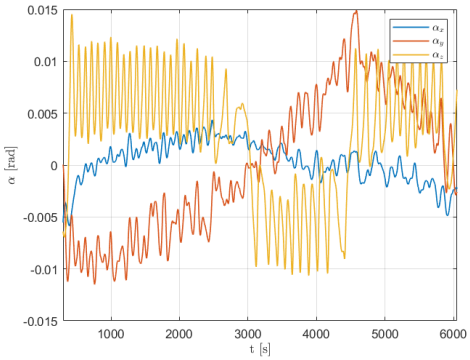

(b) Real pointing error

Figure 11: Pointing accuracy

6 Conclusions

The presented work objective was to study the attitude dynamics of a 12U Cubesat satellite in a specific operative configuration, thus designing functional control logic to complete the phases of detumbling, slew maneuver and tracking in the most effective way to obtain the required performances for a nadir pointing mission and taking into account also other constraints regarding the operational life of the spacecraft. All the analyzed tasks result to be successfully accomplished, however many limitations arose due to certain design choices such as the control error management during the tracking phase. Surely in this case, better system features could be obtained with the implementation of a Von Kalman optimal observer in order to filter more accurately the sensor noises and guarantee a proper time response of the observed state at the same time.

References

[1] L. de Maria, *Earth magnetic field with IGRF 13th gen.* 2020. [Online]. Available: `https://it.mathworks.com/matlabcentral/fileexchange/88406-earth-magnetic-field-with-igrf-13th-gen`.

[2] M. Rodríguez and J. M. Moreno, *SSOC-D60 interface control document*, Solar MEMS Technologies S.L., Oct. 2016.

[3] R. van Wyk, *Cubesense Earth Gen 2*, Revised version 1.01, CubeSpace Satellite Systems, Sep. 2023.

[4] *Stim202 3-axis gyro module data sheet*, Revised version .19.

[5] *30 mNms RW-0.03 data sheet*, Rocket Lab USA, Jul. 2021.

[6] *Vacco standard micro propulsion system*, VACCO Industries, Jun. 15.

[7] "Optimal de-tumbling of spacecraft with four thrusters," in *Proceedings of the 2019 CEAS EuroGNC conference*, CEAS-GNC-2019-051, Milan, Italy, Apr. 2019.